Surface Wind and Upper-Ocean Variability Associated with the Madden–Julian Oscillation Simulated by the Coupled Ocean–Atmosphere Mesoscale Prediction System (COAMPS)

TOSHIAKI SHINODA AND TOMMY G. JENSEN

Naval Research Laboratory, Stennis Space Center, Mississippi

MARIA FLATAU AND SUE CHEN

Naval Research Laboratory, Monterey, California

(Manuscript received 17 September 2012, in final form 3 December 2012)

ABSTRACT

Simulation of surface wind and upper-ocean variability associated with the Madden–Julian oscillation (MJO) by a regional coupled model, the Coupled Ocean–Atmosphere Mesoscale Prediction System (COAMPS), is evaluated by the comparison with in situ and satellite observations. COAMPS is configured for the tropical Indian Ocean domain with the horizontal resolution of 27 km for the atmospheric component and $1/8°$ for the ocean component. A high-resolution nested grid (9 km) for the atmospheric component is used for the central Indian Ocean. While observational data are assimilated into the atmospheric component, no data are assimilated into the ocean component. The model was integrated during 1 March–30 April 2009 when an active episode of large-scale convection associated with the MJO passed eastward across the Indian Ocean. During this MJO event, strong surface westerly winds ($\sim 8\,m\,s^{-1}$) were observed in the central equatorial Indian Ocean, and they generated a strong eastward jet ($\sim 1\,m\,s^{-1}$) on the equator. COAMPS can realistically simulate these surface wind and upper-ocean variations. The sensitivity of upper-ocean variability to the atmospheric model resolution is examined by the COAMPS experiment without the high-resolution nested grid. The equatorial jet generated in this experiment is about 20% weaker than that in the first experiment, which significantly influences upper-ocean salinity and temperature. The large diurnal warming of SST during the suppressed phase of the MJO is also adequately simulated by the model. Weak winds during this period are mostly responsible for the large SST diurnal variation based on the comparison with the spatial variation of surface forcing fields.

1. Introduction

The Madden–Julian oscillation (MJO; Madden and Julian 1972) is a major cause of intraseasonal variability in the tropics, and is associated with large-scale atmospheric circulation and tropical deep convection. Over the tropical Indian and western Pacific Oceans, anomalous atmospheric convection and surface zonal winds associated with the MJO propagate eastward at about 4–5 $m\,s^{-1}$ (e.g., Madden and Julian 1994). These surface variations provide a significant source of fluxes of momentum and heat into the ocean (e.g., Zhang 1996; Shinoda et al. 1998), that drive large upper-ocean responses, including strong equatorial currents, large fluctuation of mixed layer temperature, and changes in thermocline depths (e.g., Krishnamurti et al. 1988; Kessler et al. 1995; Ralph et al. 1997; Shinoda and Hendon 1998, 2001; Waliser et al. 2003; Shinoda et al. 2008). Also, strong diurnal variability of mixed layer temperature is observed during the suppressed phase of the MJO because of the weak winds and large shortwave radiation (Weller and Anderson 1996; Soloviev and Lukas 1997). Recent studies suggest that intraseasonal upper-ocean variability produced by the MJO plays an important role in tropical interannual variations such as the Indian Ocean dipole (IOD; Saji et al. 1999) and ENSO (e.g., McPhaden and Yu 1999, Kessler and Kleeman 2000, Shinoda and Han 2005, Han et al. 2006), and thus an accurate simulation of the MJO and associated ocean variability is crucial for prediction of tropical weather and climate.

Corresponding author address: Toshiaki Shinoda, Naval Research Laboratory, Stennis Space Center, MS 39529.
E-mail: toshiaki.shinoda@nrlssc.navy.mil

DOI: 10.1175/MWR-D-12-00273.1

Despite the importance of the MJO for tropical and extratropical climate variability, most state-of-the-art coupled general circulation models (CGCMs) are unable to simulate any of its salient features (Lin et al. 2006; Hung et al. 2013). For example, intraseasonal variance of eastward propagation in most models is too weak, and the highly coherent eastward propagation of convection and surface winds is not clearly evident. Although a MJO simulation in some of the more recent versions of CGCMs have been improved (e.g., Subramanian et al. 2011), the models can simulate fundamental features of the MJO only qualitatively, and substantial model improvement is still required for the quantitative comparison with in situ observations.

Ocean response to surface forcing produced by the MJO is investigated with a variety of observational and modeling studies (e.g., Kessler et al. 1995; Shinoda and Hendon 2001; Roundy and Kiladis 2006; Sengupta et al. 2007; see also the review article of Kessler 2005). Because of the improvement of satellite-derived surface forcing fields in recent years, current state-of-the-art ocean general circulation models (OGCMs) are able to simulate oceanic intraseasonal variability associated with the MJO at least qualitatively. For example, Sengupta et al. (2007) demonstrated that an ocean model forced with the Quick Scatterometer (QuikSCAT) surface winds can simulate intraseasonal variability of the eastward equatorial jets associated with westerly wind events over the Indian Ocean reasonably well. However, there are still significant discrepancies between the in situ data and model results during certain periods, which are primarily attributed to the error of QuikSCAT surface wind stress (Sengupta et al. 2007). For example, westerly wind events in the warm pool region measured by QuikSCAT tend to be stronger than those of in situ observations during some MJO events (Shinoda et al. 2008).

While satellite-derived surface forcing fields are available in recent years, long-term integrations of OGCM still require the use of surface fluxes from reanalysis products. Also, operational ocean nowcast/forecast systems have to be forced with global atmospheric analysis products or predicted fields by atmospheric models because the satellite-derived surface forcing fields are not available in real time. Global analysis products generally produce major features of the MJO including the coherent eastward propagation of surface winds and convection over the tropical Indian and western Pacific Oceans (e.g., Shinoda et al. 1999; Weaver et al. 2011). However, significant errors in MJO variability are found in these analyses when compared with in situ observations. For example, strong

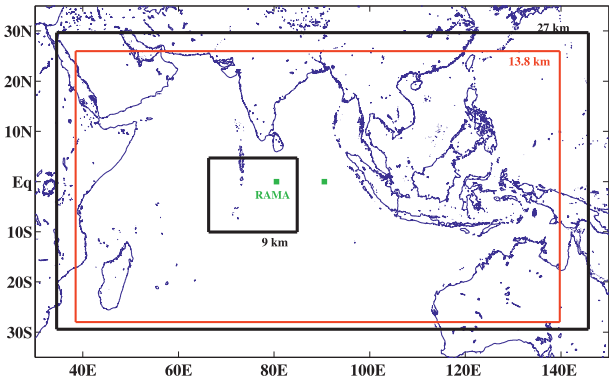

FIG. 1. Model domain and the horizontal resolutions of atmospheric (black rectangles) and ocean (red rectangle) components of COAMPS.

westerly wind events associated with the MJO are not necessarily reproduced well (e.g., Shinoda et al. 1999, 2008). These errors could partly be attributed to the coarse resolution of the global assimilation system. When ocean models are forced with surface forcing fields derived from atmospheric analysis products, significant errors are found in simulated upper-ocean intraseasonal variability associated with the MJO, including surface currents, thermocline depths, and the amplitude of Kelvin waves (e.g., Sengupta et al. 2007; Shinoda et al. 2008).

In this study, a high-resolution regional coupled model is used to simulate the atmospheric and oceanic variability associated with the MJO. The model is configured for the tropical Indian Ocean where relatively few comparisons of model MJO variability with in situ observations are performed in past studies. Atmospheric data are assimilated into the regional model, which uses much finer resolution than global analysis products. Also, the ocean component uses high horizontal and vertical resolutions. A major focus of the present study is on oceanic variability associated with the MJO. Particular emphasis is given to the sensitivity of upper-ocean variability to the atmospheric model resolution. We demonstrate the importance of the use of high-resolution atmospheric model for simulating the strong oceanic equatorial jet associated with the MJO based on the comparison of the Coupled Ocean–Atmosphere Mesoscale Prediction System (COAMPS) experiments with different atmospheric model resolutions. Compared to other coupled and ocean GCM studies, the model uses the exceptionally fine vertical resolution in the upper 10 m in the ocean component, and thus the model is able to well represent the diurnal warming. The spatial pattern of large diurnal warming during the suppressed phase of the MJO is described, and it is compared with surface forcing fields.

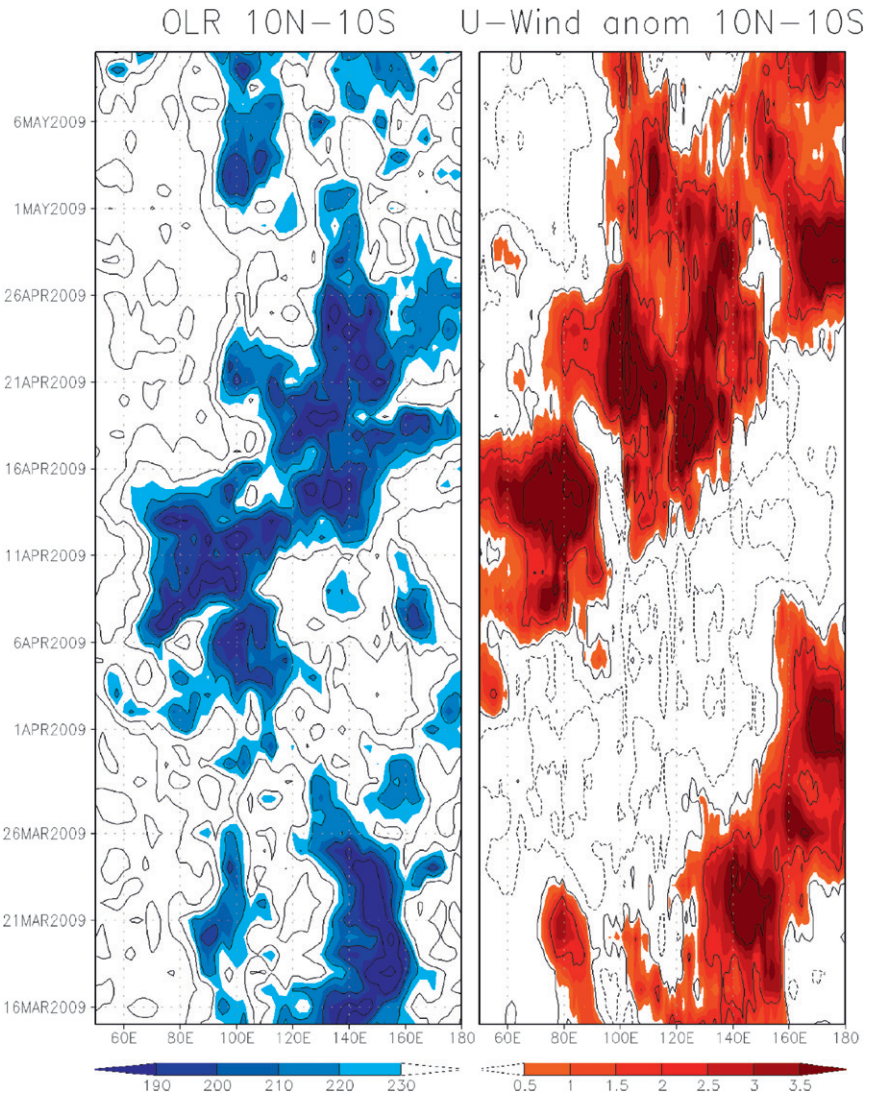

FIG. 2. (left) A longitude–time diagram of OLR averaged over 10°N–10°S. (right) As in (left), but for the zonal wind anomaly derived from QuikSCAT.

2. Model and experiments

a. COAMPS

Model simulations are performed with COAMPS. As the general description of COAMPS is detailed in other papers (Hodur 1997; Chen et al. 2003, 2010), the aspects most relevant to the present study are briefly described in this section. Figure 1 describes the model resolutions and domain that covers the almost entire tropical Indian Ocean and Maritime Continent.

The ocean component is the hydrostatic Navy Coastal Ocean Model (NCOM), which uses a combination of terrain-following sigma and z-level coordinates (Martin 2000; Martin et al. 2006). The model is based on the Princeton Ocean Model (Blumberg and Mellor 1987) and also includes a free surface. The atmospheric component is a terrain-following sigma coordinate, nonhydrostatic model (Hodur 1997; Chen et al. 2003). The ocean and atmospheric components are coupled using the Earth System Modeling Framework (ESMF; http://www.earthsystemmodeling.org/). The atmosphere has two nests of horizontal spacing, 27 and 9 km, each nest having 40 layers in vertical. The inner nest is located in the central Indian Ocean near the equator (10°S–5°N, 66°–85°E) where strong zonal winds associated with the MJO are often observed. The single-moment bulk microphysics prediction scheme (Rutledge and Hobbs 1983) with recent ice and thermodynamics upgrades (J. Schmidt 2011, personal communication) is used in the entire model domain. The cumulus parameterization

(Kain and Fritsch 1990, 1993) is used only outside of the inner nest where the horizontal resolution is 27 km.

The horizontal resolution of the ocean component is 1/8°, with 60 layers in vertical. In particular, an exceptionally fine vertical spacing (0.5 m) is used in upper 10 m to resolve the large diurnal warming, which is primarily observed in the upper few meters. The initial and lateral boundary conditions for the atmospheric model come from 6-hourly output of the Navy Operational Global Atmospheric Prediction System (NOGAPS; Hogan and Rosmond 1991) with the 0.5° horizontal resolution, and those for the ocean model come from the 6-hourly output of the global NCOM, with the 1/8° horizontal resolution (Barron et al. 2006).

Data assimilation is performed for the atmospheric component using the Navy Atmospheric Variational Data Assimilation System (NAVDAS; Daley and Barker 2001). It creates a new initial analyzed field every 12 h, at 0000 and 1200 UTC every day (Hodur 1997; Chen et al. 2003, 2010). The model then runs forward for 12 h in hindcast mode to repeat the cycle. There is no data assimilation for the ocean component, and thus the simulation of the ocean is constrained only by the initial, surface, and lateral boundary conditions. Further details of COAMPS that include the assimilation method, physical scheme, and air–sea coupling technique are found in Chen et al. (2003, 2010, 2011) and Jensen et al. (2011).

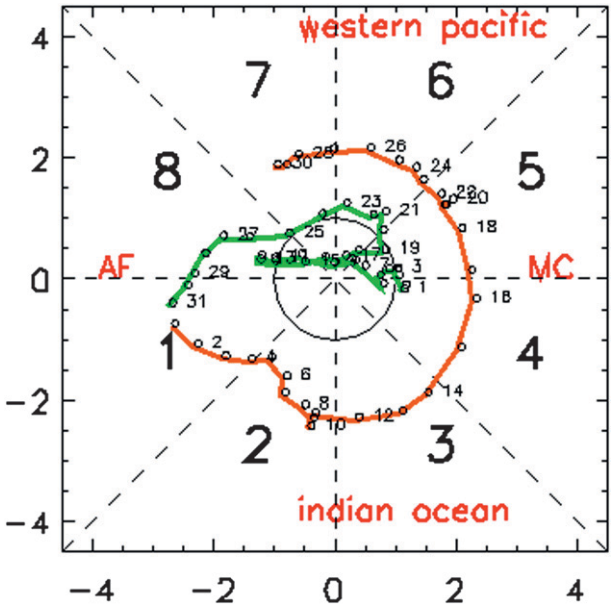

FIG. 3. MJO index defined by Wheeler and Hendon (2004) for the period 1 Mar–30 Apr 2009. Green (red) lines indicate March (April).

b. *MJO event in spring 2009 and the model simulation*

Figure 2 shows the outgoing longwave radiation (OLR; Liebmann and Smith 1996) and zonal wind anomaly at 10 m near the equator (10°N–10°S) calculated from

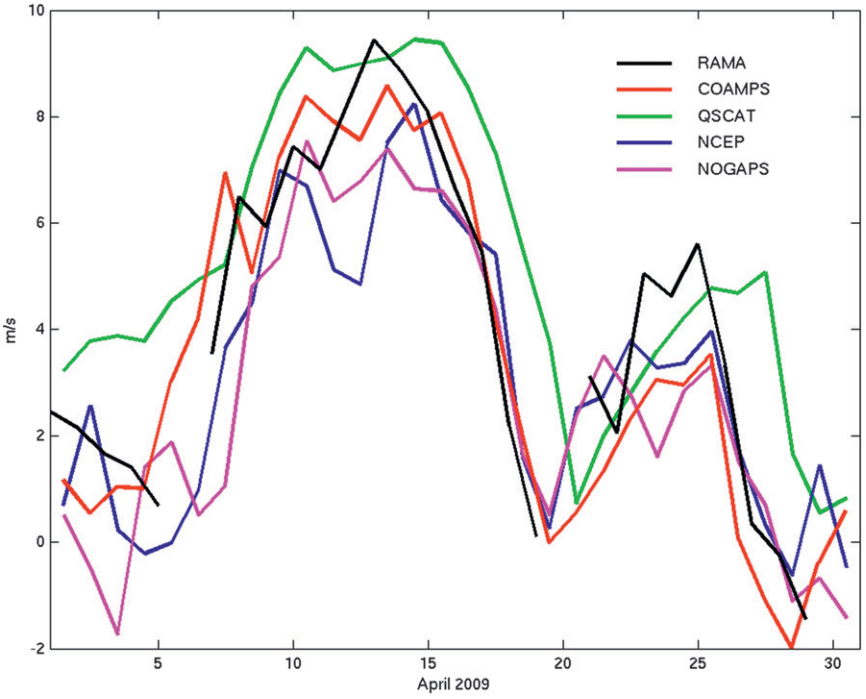

FIG. 4. Daily mean 10-m height zonal winds at 0°, 80.5°E during April 2009 from the RAMA buoy, COAMPS, QuikSCAT, the NCEP–NCAR reanalysis, and NOGAPS.

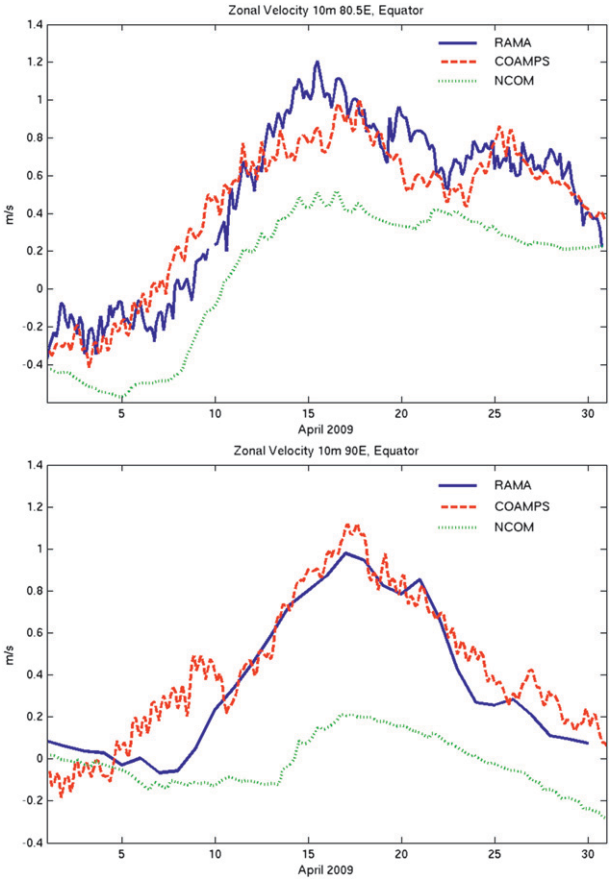

FIG. 5. Zonal velocity at 10-m depth during April at (top) 0°, 80.5°E and (bottom) 0°, 90°E from the RAMA buoy (solid blue line), COAMPS (dashed red line), and the global NCOM (dotted green line).

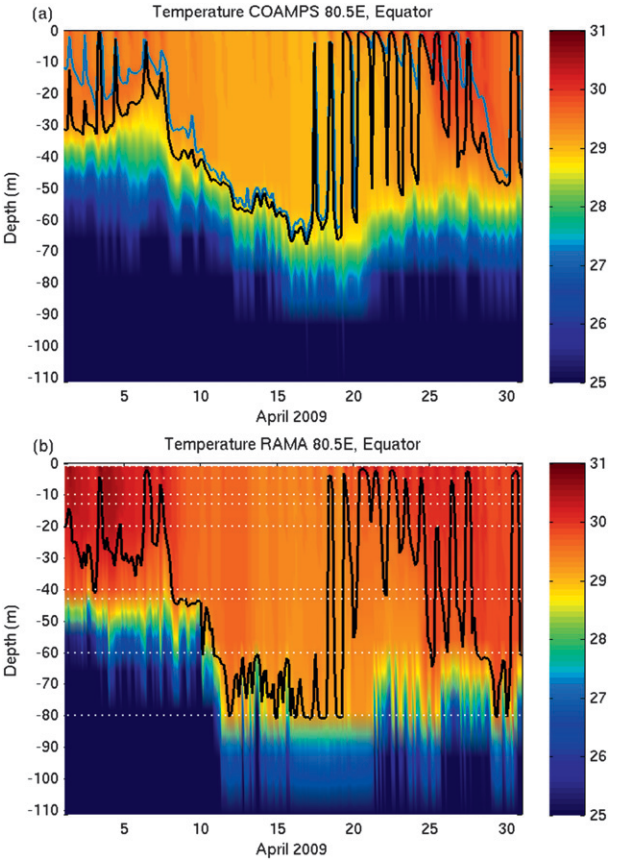

FIG. 6. (a) Temperature (shading) at 0°, 80.5°E during April 2009 from COAMPS. The light blue solid line indicates the mixed layer depth and the black solid line indicates the top of the thermocline depth (see text for the detail). (b) As in (a), but for the temperature from the RAMA buoy. The white dotted lines indicate the depth of the instrument.

QuikSCAT data [see also section 2c(2)]. During mid-March, the active atmospheric convection was found in the western Pacific, and the convection moved westward in late March. The active convection associated with the MJO in the central Indian Ocean was initiated around 6 April and propagated eastward in mid-April. In association with the active convection, strong westerly winds were generated in the central Indian Ocean during 10–16 April around 60°–85°E. After 16 April, atmospheric convection was largely suppressed in the Indian Ocean west of 90°E, and winds became much weaker. Large-scale active convection and westerly winds were moved to the western Pacific by late April. The MJO index defined by Wheeler and Hendon (2004) indicates high values during late March to the end of April 2009 (Fig. 3). Since strong westerly wind events near the equator over the Indian Ocean during this period are observed, this event is suitable for evaluating the model's ability to simulate large upper-ocean variability that includes the generation of strong equatorial currents and the rapid deepening of the mixed layer during the active phase of the MJO.

To simulate oceanic and atmospheric variability associated with the MJO event described above, COAMPS is integrated for the period 1 March–30 April 2009 (hereafter referred to as control experiment). To investigate the sensitivity of the results to the atmospheric model resolution, an additional experiment without the inner nest of the atmosphere is performed (referred to as EX-1). EX-1 uses the cumulus parameterization (Kain and Fritsch 1990) in the entire model domain where the horizontal resolution is more than 10 km.

c. Observational data and analysis products for the model evaluation

1) RAMA BUOY DATA

In situ data from the Research Moored Array for African–Asian–Australian Monsoon Analysis and Prediction (RAMA) program (McPhaden et al. 2009)

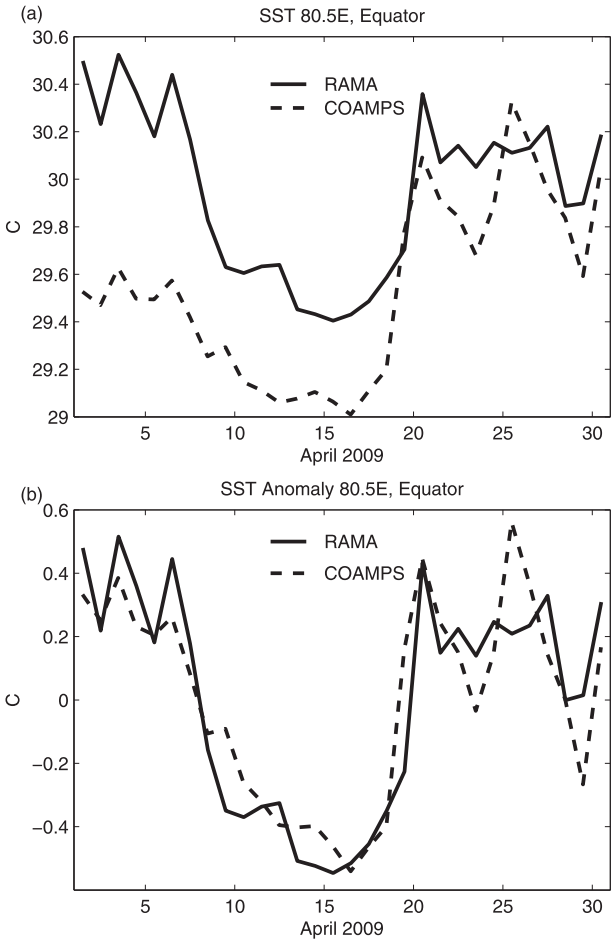

FIG. 7. (a) Daily mean SST at 0°, 80.5°E from the RAMA buoy (solid line) and COAMPS (dashed line). (b) As in (a), but the linear trend is removed and the mean is subtracted.

are used to evaluate the COAMPS simulations. A major focus of the evaluation is on the strong westerly winds and oceanic equatorial jet during the active phase of the MJO. Both surface winds (10-min interval) at 4-m height and near-surface ocean currents (20-min interval) at 10-m depth are available at 0°, 80.5°E during the entire period of the COAMPS simulation. The time series of temperature profile (10-min interval) at the same location are used to compare the mixed layer evolution by the strong winds. The daily mean near-surface currents at 0°, 90°E are also available, which are used to evaluate the simulation of the equatorial jet. Note that the wind data at 0°, 90°E are missing for the period of the simulation.

2) QUIKSCAT WINDS

Winds at 10-m height derived from the SeaWinds QuikSCAT measurements obtained from the Remote Sensing Systems website (www.remss.com) are analyzed. We use the daily data with 1° grid spacing to compare the large-scale wind variation during the active phase of the MJO with the COAMPS simulations.

3) GLOBAL ATMOSPHERIC ANALYSIS PRODUCTS

While near-surface atmospheric variables can be obtained from a number of global analysis products in recent years, we use two specific products which are widely used for examining atmospheric processes and forcing operational ocean forecast systems. These are the National Centers for Environmental Prediction–National Center for Atmospheric Research (NCEP–NCAR) reanalysis (Kalnay et al. 1996) and NOGAPS (Hogan and Rosmond 1991). The NCEP–NCAR reanalysis has been used for a wide range of research on atmospheric processes during the last decade because they provide 60 yr of homogeneous data with no spurious discontinuities due to changes in the assimilation scheme. We use the daily surface wind data with Gaussian grid at T62 spectral truncation.

NOGAPS is a global spectral numerical weather prediction model, and it has been used operationally at the Fleet Numerical Meteorology and Oceanography Center (FNMOC) since 1994. The model resolution is at T239 spectral truncation with 30 layers in vertical. Further details of the model and assimilation method are found in Hogan and Rosmond (1991), Rosmond (1992), and Goerss and Phoebus (1992). The current Navy's operational global ocean nowcast/forecast system uses NCOM forced with near-surface atmospheric variables from NOGAPS (Barron et al. 2004, 2006). Since the ocean component of COAMPS is also NCOM, surface wind fields from NOGAPS and ocean variability from the global NCOM simulation with NOGAPS surface forcing is compared with the COAMPS simulation. While there are a number of other global atmospheric analysis products, the comparison between those multiple datasets is beyond the scope of this paper.

3. Results

a. Validation of the model simulation

Surface wind and upper-ocean variability from the control experiment (CR) during the entire April 2009 is compared with in situ and satellite observations and global analysis products. The period covers both the active (10–16 April) and suppressed (1–5, 20–30 April) phases of the MJO in the central and eastern Indian Ocean.

Figure 4 shows the daily mean zonal winds at 10 m at 0°, 80.5°E from the RAMA buoy, COAMPS-CR simulation, QuikSCAT, the NCEP–NCAR reanalysis, and

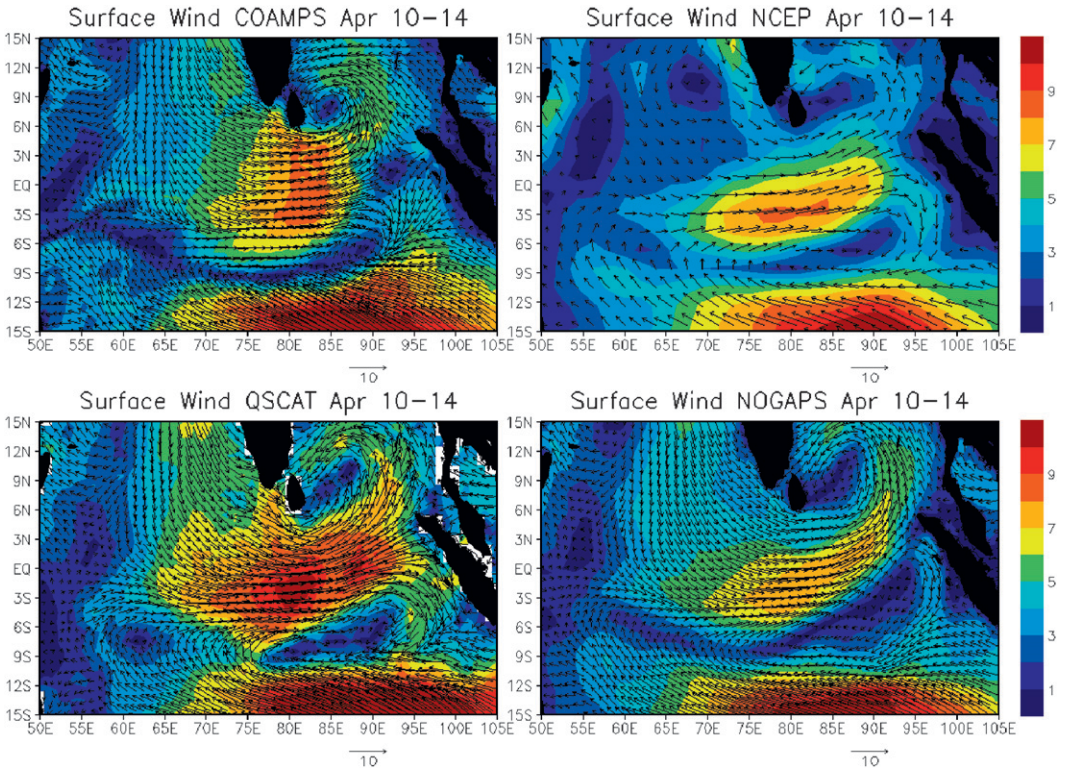

FIG. 8. Average surface wind (arrows) and wind speed (shading) during 10–14 Apr 2009 from (top left) COAMPS, (bottom left) QuikSCAT, (top right) the NCEP–NCAR reanalysis, and (bottom right) NOGAPS.

NOGAPS analysis. Zonal winds at 4 m measured by the RAMA buoy are extrapolated to 10 m using air temperature, humidity at 2 m, and SST with the Tropical Ocean and Global Atmosphere Coupled Ocean–Atmosphere Response Experiment (TOGA COARE) bulk flux algorithm, version 3.0 (Fairall et al. 1996).

The large variation of zonal wind associated with the MJO is observed by the RAMA buoy. During early

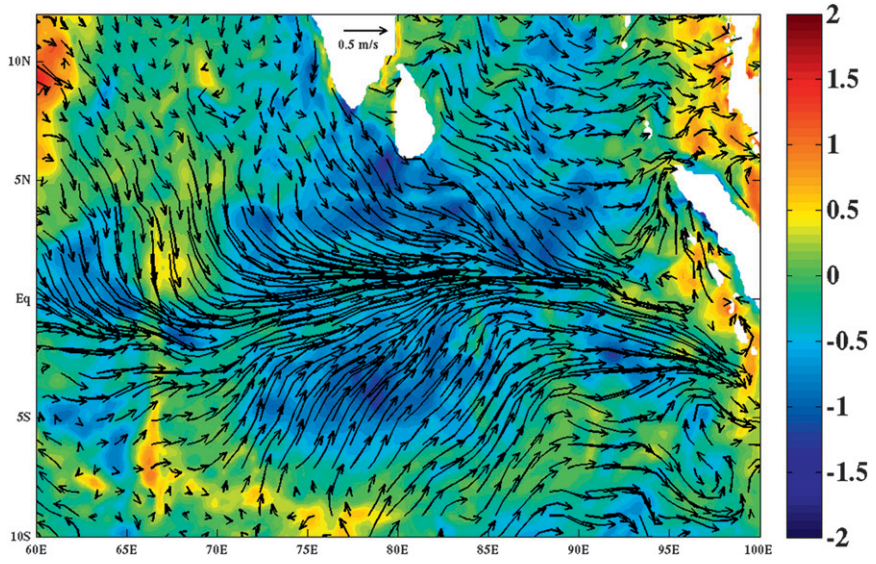

FIG. 9. Average surface current (arrows) and SST (shading) anomalies during 15–17 Apr 2009 relative to the mean of 1–5 Apr.

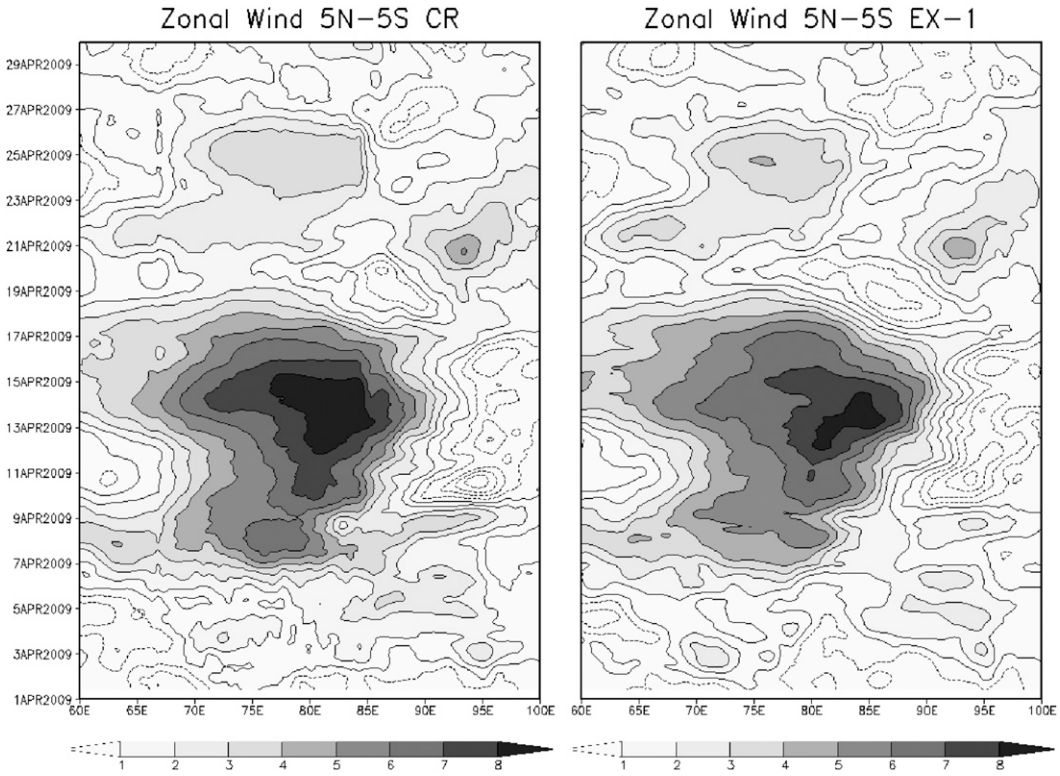

FIG. 10. A longitude–time diagram of zonal wind at 10 m averaged over 5°N–5°S from (left) CR and (right) EX-1. The atmospheric component of CR uses the high-resolution nested grid (9 km) in the central equatorial Indian Ocean, while the course horizontal resolution (27 km) is used in the same area for EX-1 (see text for the detail).

April the daily mean zonal winds are weaker than $2\,m\,s^{-1}$ most of the time. Then westerly winds are accelerated in 6–9 April, and the strongest westerlies about $7–9\,m\,s^{-1}$ are observed during 10–15 April. The winds then become weak quickly in 16–19 April. All other time series in Fig. 4 show similar variations. In fact, there is no significant difference in the correlation coefficient r with the RAMA buoy data ($r = 0.90$ for COAMPS, $r = 0.91$ for NCEP, $r = 0.87$ for QuikSCAT, $r = 0.91$ for NOGAPS). However, there are significant differences in the strength of the zonal wind during the active phase. While the zonal winds during 10–15 April simulated by COAMPS shows similar strength to that in the RAMA buoy, QuikSCAT winds are stronger and winds from the NECP–NCAR reanalysis and NOGAPS are weaker. This result is consistent with previous studies on the western tropical Pacific wind variation, in which westerlies from QuikSCAT (the NCEP–NCAR reanalysis) tend to be stronger (weaker) than in situ observations during the active phase of the MJO (e.g., Shinoda et al. 2008).

The near-surface (10-m depth) zonal currents at 0°, 80.5°E and 0°, 90°E from the RAMA buoy, the COAMPS simulation, and the global NCOM simulation during April 2009 are shown in Fig. 5. Ocean data are assimilated in the global NCOM simulation based on the Modular Ocean Data Assimilation System (MODAS; Fox et al. 2002), while there is no data assimilation in the ocean component of COAMPS. The RAMA buoy data show that strong eastward jets are generated in both locations in response to the strong westerly winds (Yoshida 1959). The maximum zonal current exceeds $1\,m\,s^{-1}$ at 80.5°E near the end of the active phase. COAMPS is able to simulate the generation of the strong equatorial jet produced by the MJO very well. Although the global NCOM generates the equatorial jet at 0°, 80.5°E during the same period, it is much weaker than observations. The strong equatorial jet is not evident at 0°, 90°E in the global NCOM simulation. These differences between models and observations are attributed to the error of the equatorial westerly winds, which will be further elaborated on in the following sections.

Figure 6 displays the upper-ocean temperature and mixed layer variations associated with the MJO event. The mixed layer depth (light blue lines in Fig. 6) is defined as the depth at which density increases by Δd above the surface value. Here, Δd is specified to be equivalent to the density increase produced by a 0.3°C decrease in

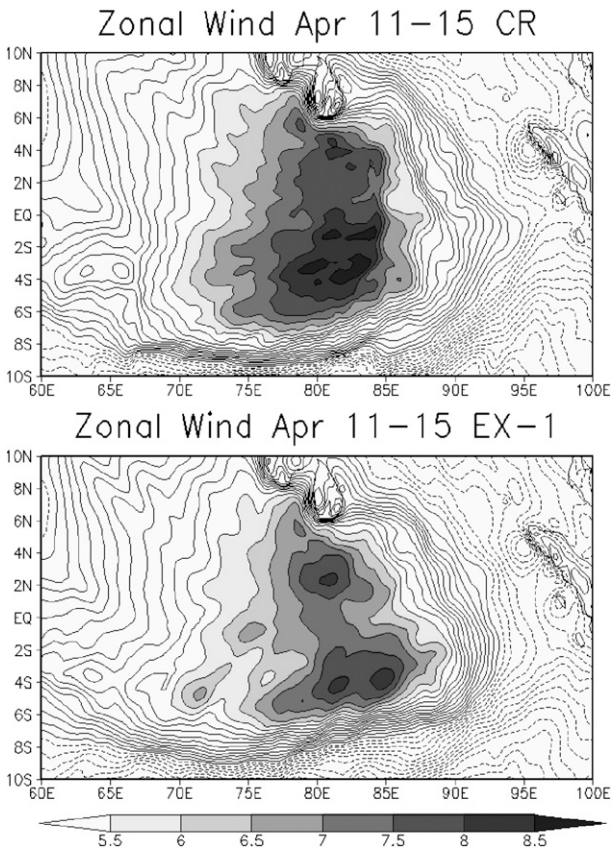

FIG. 11. Average zonal wind at 10 m during 11–15 Apr 2009 from CR and EX-1.

temperature from the surface value, but with the salinity held constant at the surface value. The top of the thermocline depth (black lines in Fig. 6) is defined as the depth at which temperature decreases by ΔT above the surface value. ΔT is specified to be 0.3°C. Although temperature records at all depths of the instrument (dotted lines in Fig. 6b) are available for the time interval of 10 min, the salinity data of the same time interval are only available at depths 20 m or deeper. Therefore, the mixed layer depth, which is often less than 20 m, is not included in Fig. 6b.

During the suppressed phase in early April, the mixed layer depth is about 10–20 m and the top of the thermocline depth is about 30 m in the COAMPS simulation. Therefore, 10–20-m thickness of barrier layer, which is defined as the isothermal layer below the mixed layer (Lukas and Lindstrom 1991), is evident during this period. Then the rapid deepening of the mixed layer is produced by the strong westerly winds during the active phase, and the mixed layer is about 70 m during 16–17 April. The barrier layer is eroded by the strong wind event. Then the mixed layer becomes very shallow during the suppressed phase after 18 April when the surface wind is very weak. A large diurnal variation of the mixed layer depth is found during this period. Since the temperature stratification in the upper 50 m is already very weak in late April due to the strong mixing that occurred during the active phase, the subsequent relatively weak westerlies cause the significant deepening of the mixed layer in late April.

This mixed layer evolution simulated by COAMPS is consistent with observations. The top of the thermocline depth in early April calculated from the RAMA buoy data is about 30 m. Then the subsequent strong mixing causes the mixed layer to be deeper to about 60–80 m. Then the large diurnal variation is observed during the suppressed phase. While the overall agreement between the COAMPS simulation and in situ observations is evident, significant discrepancies in the mixed layer depth are found during the active phase. The mixed layer appears to be deeper in the observations. However, a further quantitative comparison is difficult because of the insufficient vertical resolution of the observations. For example, there is no instrument between 60 and 80 m, and thus the variation of the deep mixed layer (~70 m) during mid-April simulated by COAMPS is not well resolved by the RAMA buoy data. Nevertheless, the comparison suggests that COAMPS is able to simulate the rapid deepening of the mixed layer caused by strong westerly wind event associated with the MJO reasonably well.

Figure 7a shows SST time series from the COAMPS simulation and RAMA buoy. Although the variation is similar in both time series, there are significant differences in the time mean and longer time-scale variability. To examine anomalous SST caused by convection and winds associated with the MJO, the linear (longer time scale) trend is removed and the mean is subtracted from the time series (Fig. 7b). The warming trend in COAMPS can partly be attributed to the error of the initial upper-ocean temperature derived from the global NCOM analysis. The SST variation associated with MJO convection agrees well with the observation, especially the large cooling (~0.9°C) during the active phase and the subsequent rapid warming during the suppressed phase.

In summary, COAMPS is able to realistically simulate the surface winds and upper- ocean variability associated with the MJO near the equator observed by the RAMA buoy including strong westerly winds, surface ocean currents, and rapid mixed layer deepening and subsequent recovery. In particular, the acceleration of strong equatorial jets that exceed 1 m s^{-1} is simulated by the model very well. However, there are some significant differences between the model simulation and observations such as the mixed layer depth during the

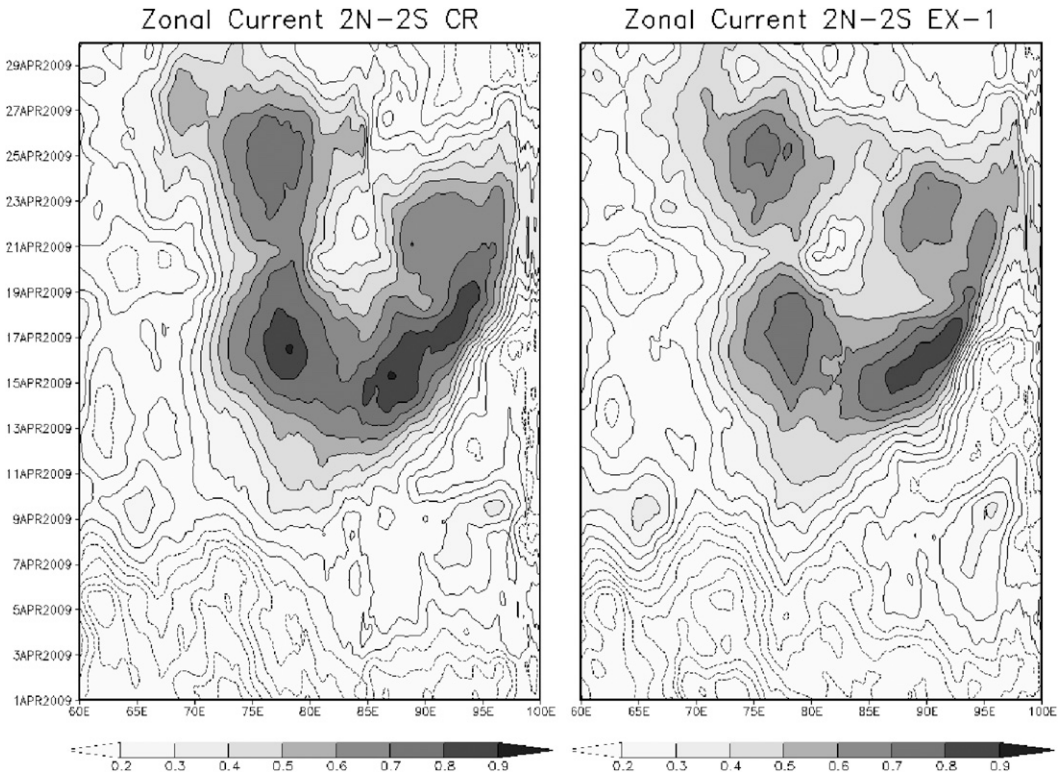

FIG. 12. A longitude–time diagram of surface zonal current averaged over 2°N–2°S from (left) CR and (right) EX-1.

active phase. Such differences are expected to some extent since the observed data at one location include variability caused by small-scale atmospheric convection and wind variations that cannot be resolved by the atmospheric model (9-km resolution) as well as mesoscale and submesoscale oceanic eddies that are not generally predictable by models.

b. Large-scale variability

1) SURFACE WIND

The spatial variation of surface winds during the active phase of the MJO simulated by COAMPS is described and compared with satellite data and global analysis products (Fig. 8). The large-scale pattern of surface wind is quite similar in all datasets. Strong westerly winds are centered around 3°S, 80°–85°E, which are associated with the cyclonic circulation in the Bay of Bengal east of Sri Lanka. Westerly winds are evident between 6°N and 8°S around 65°–90°E in all datasets, but the strength of the westerly is notably different. The westerlies in COAMPS are weaker than those in QuikSCAT and stronger than those in NECP–NCAR reanalysis and NOGAPS, which is consistent with the comparison at 0°, 80.5°E (Fig. 4). The good agreement for the spatial pattern suggests that westerly winds simulated by COAMPS, which are validated by the comparison at one location, are realistic for the larger scale in the tropical Indian Ocean.

2) SURFACE CURRENT AND SST

Figure 9 shows surface current and SST difference between periods near the end of the active phase (15–17 April) and suppressed phase (1–5 April) before the active phase. Strong equatorial jets with large zonal extent (60°E–the eastern boundary) are generated by the strong westerlies during the active phase. The strongest zonal jets are located around 80°–90°E, and they are associated with meridional convergence. Significant cooling is evident in almost the entire tropical Indian Ocean. In particular, large cooling (>0.5°C) is found near the equator (5°N–7°S) east of 70°E. An anomalous warming is found near the eastern boundary.

c. Sensitivity of ocean variability to atmospheric model resolution

The results from the control experiment (CR) indicate that the strong westerly winds associated with the MJO are generated near the equator around 80°–85°E where the high-resolution nested grid is used for the atmospheric component. The strength of the winds around

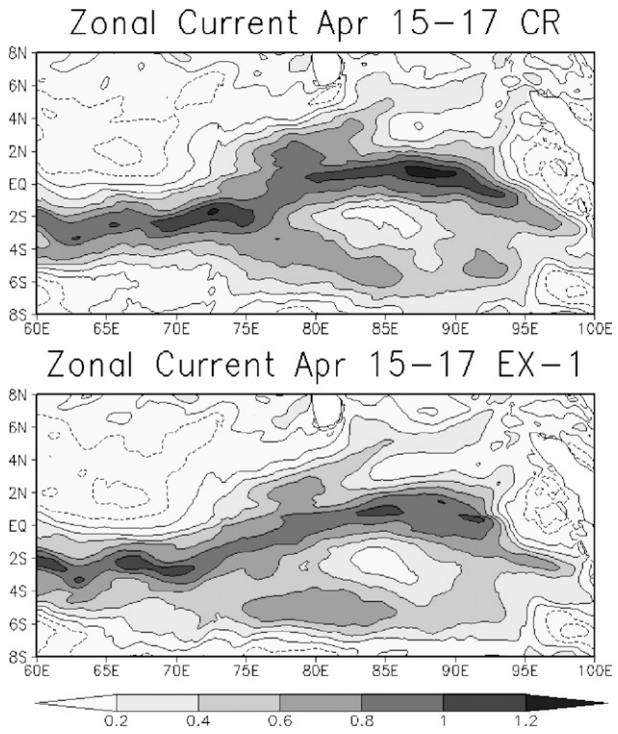

FIG. 13. Average surface zonal current during 15–17 Apr 2009 from (top) CR and (bottom) EX-1.

this region may largely affect the equatorial jet, and thus the accurate simulation of winds in the region of nested grid is crucial for generating realistic equatorial ocean currents. In this section, the sensitivity of upper-ocean variability to the atmospheric model resolution is discussed based on the comparison between CR and EX-1.

Figure 10 shows the zonal wind variation near the equator from CR and EX-1. While the time evolution and location of strong westerlies are similar in the two experiments, the strength of the zonal wind is significantly different. The control experiment generates stronger westerlies during the active phase of the MJO than EX-1. The difference is particularly prominent in the area 4°N–6°S, 77°–85°E (Fig. 11). These are the areas where the high-resolution nested grid is used for the atmosphere. The difference in maximum wind around this region is about $0.5\,\mathrm{m\,s^{-1}}$.

The difference in the strength of westerlies during the active phase can largely influence the equatorial oceanic jet. Figure 12 shows the zonal current near the equator. The time evolution and location of jets are similar in the two experiments, but those in CR is significantly stronger than EX-1. The maximum zonal current in CR near the end of active phase is about $0.2\,\mathrm{m\,s^{-1}}$ stronger than that in EX-1 (Fig. 13). This difference is about 20% of the equatorial jet velocity simulated by CR during this period.

The difference in surface winds and upper-ocean currents may cause differences in salinity and temperature through horizontal advection, vertical mixing, and surface heat and freshwater fluxes. Figure 14 shows the salinity and temperature in the central equatorial Indian Ocean in CR and EX-1 before the generation of strong equatorial jet and after the active phase when strongest jet is simulated. During the suppressed phase, upper-ocean temperature and salinity are similar in the two experiments. After the active phase, much deeper mixed layers near the equator are found in both CR and EX-1. However, the mixed layer salinity and temperature are significantly different in the two experiments. In particular, the large difference in salinity is evident. The mixed layer salinity near the equator in CR is much higher (~0.4 psu) than EX-1. This difference is caused by a combination of horizontal salinity advection, stronger vertical mixing, and surface freshwater flux.

Although the stronger mixing in CR may affect the upper-ocean salinity in this region through the entrainment of saltier waters below the mixed layer, the mixed layer depth in the two experiments are not substantially different. Hence, horizontal advection may also contribute to the difference in the two experiments. In the equatorial central Indian Ocean, zonal current variation strongly influences the upper-ocean salinity because of the large zonal gradient of surface salinity (Jensen 2001; Schott and McCreary 2001; Grunseich et al. 2011). Figure 15 displays surface currents and salinity from CR and EX-1 near the end of the active phase. The eastward intrusion of high salinity waters from the Arabian Sea is more prominent in CR because of the stronger eastward jet.

Previous studies indicate that upper-ocean salinity stratification in the tropics could largely influence the mixed layer processes and thus SST (e.g., Lukas and Lindstrom 1991; Sprintall and Tomczak 1992; Shinoda and Lukas 1995; Han et al. 2001; Maes et al. 2005). While SST in the central and eastern tropical Indian Ocean are directly controlled by surface heat flux, vertical mixing, and heat advection, the upper-ocean salinity variation may also influence SST through affecting the entrainment heat flux due to the barrier layer formation and erosion. The results suggest that the accurate simulation of surface zonal winds near the equator and oceanic equatorial jets are also crucial to simulate upper-ocean salinity realistically. Further thorough analyses are necessary to quantify the relative importance of a variety of oceanic and atmospheric processes for controlling the temperature and salinity in the central and eastern Indian Ocean including the role of salinity in vertical mixing.

Although the spatial pattern of surface winds in COAMPS is similar to other datasets (Fig. 8), the zonal

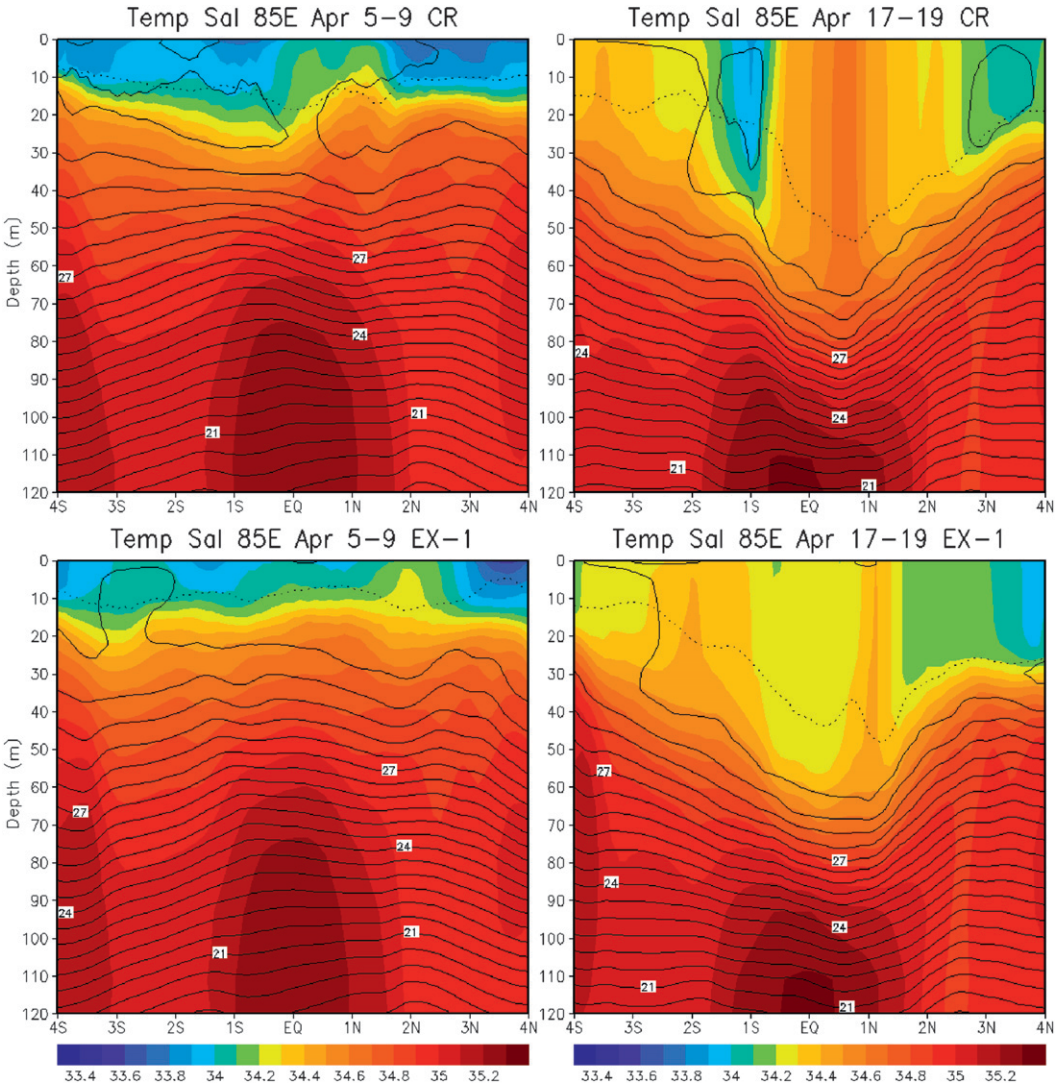

FIG. 14. Latitude–depth cross section of temperature (contour) and salinity (shading) at 85°E between 4°N and 4°S during 1–5 Apr from (top left) CR and (bottom left) EX-1, and during 17–19 Apr from (top right) CR and (bottom right) EX-1. Dotted lines indicate the mixed layer depth.

extent of strong westerlies near the equator is smaller. In particular, westerly winds in COAMPS are weaker east of 85°E where the high-resolution nested grid is not used. The results of the two experiments (CR and EX-1) suggest that a high-resolution atmospheric model tends to generate stronger westerlies associated with MJO convection. Hence, the use of nested grid for the larger area that includes east of 85°E may further improve the model simulation of strong westerly winds during the active phase.

While it is difficult to identify a variety of atmospheric processes that cause stronger westerlies in CR based only on the analysis conducted in this study, it is likely that the difference in westerly winds is relevant to the difference in atmospheric convection and precipitation between the two experiments, which use the different representations of moist physics. Our analysis indicates that precipitation in the area of nested grid during the active phase of the MJO in CR is significantly higher than that in EX-1 (not shown). Further model diagnoses that focus on moist processes associated with strong MJO convection are necessary to demonstrate how exactly stronger westerlies are generated within the high-resolution nested area by atmospheric processes.

d. Diurnal cycle

During the suppressed phase of the MJO, strong diurnal warming is observed in the tropical Indian and

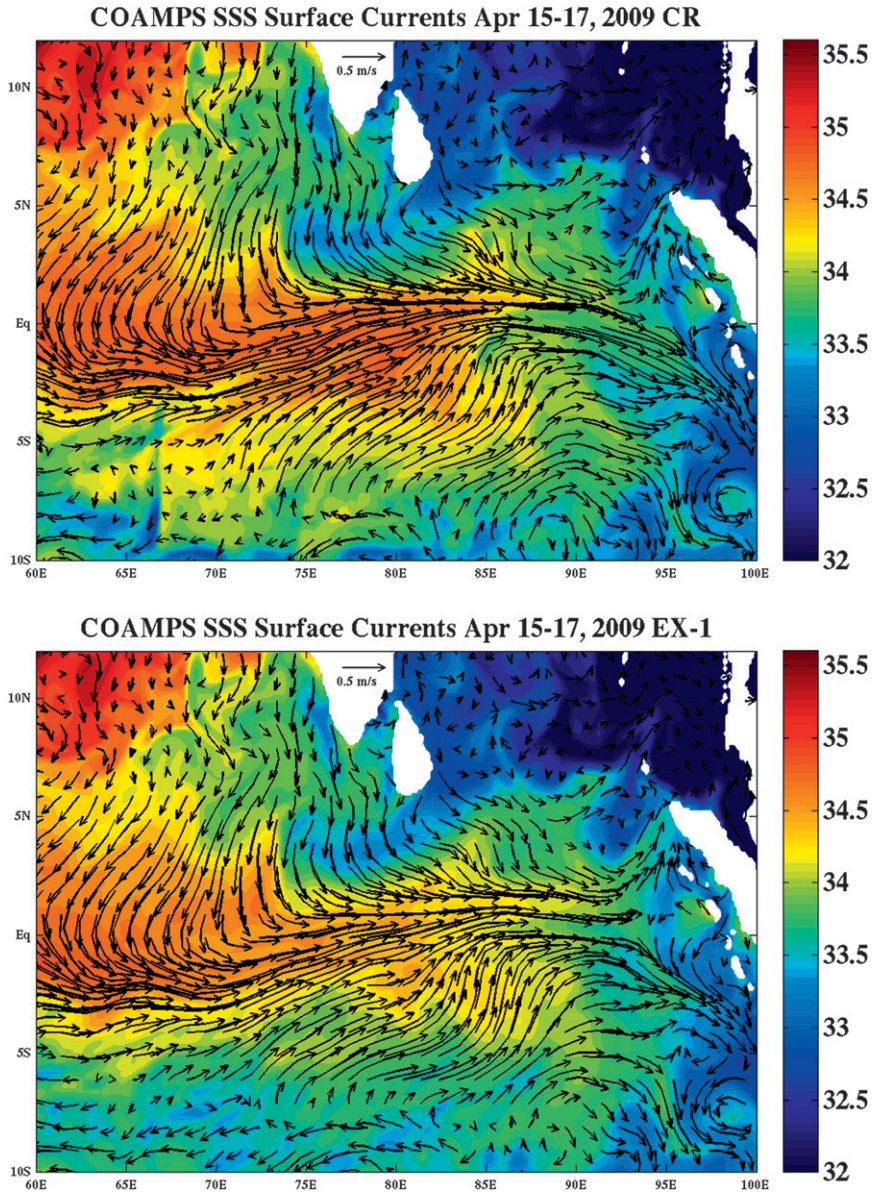

FIG. 15. Average surface current (arrows) and salinity (shading) during 15–17 Apr 2009 from (top) CR and (bottom) EX-1.

western Pacific Oceans (e.g., Weller and Anderson 1996; Soloviev and Lukas 1997; Bellenger and Duvel 2009). The diurnal cycle of the solar radiation modulates intraseasonal SST variability (e.g., Shinoda and Hendon 1998; Shinoda 2005), and thus it could feedback on atmospheric convection for the intraseasonal time scale, and its inclusion in coupled models may improve the MJO forecast (Woolnough et al. 2007).

Because the ocean component of COAMPS used in this study employs exceptionally fine vertical spacing (0.5 m) in the upper 10 m, the large diurnal warming, which occurs mostly in the upper few meters, can be adequately resolved. Figure 16 shows time series of temperature at 0 and 1 m from CR and at 1 m from the RAMA buoy observation. During the suppressed phase of the MJO, the large (1°–1.5°C) diurnal warming is often observed. COAMPS is able to generate the realistic large diurnal warming observed during this period. However, individual warming in each day in the model does not agree well with observations. This is partly due to the difference in surface shortwave radiation caused by the small-scale cloud variability, which cannot be resolved by the atmospheric model. Also, small vertical movement of the instrument causes large difference in

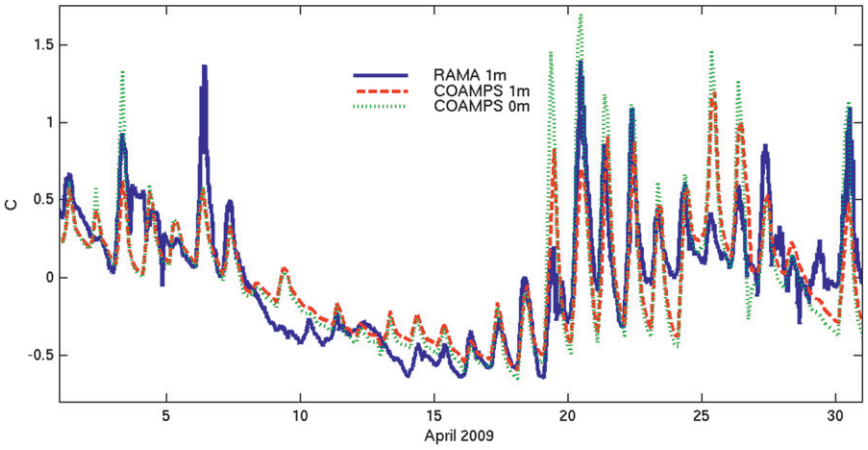

FIG. 16. Temperature anomaly at 1-m depth at 0°, 80.5°E from the RAMA buoy (solid line) and COAMPS (dashed line) and at 0 m from COAMPS (dotted line). The linear trend is removed and the mean is subtracted.

observed temperature because of the large vertical temperature gradient in the near-surface layer. In fact, the notable difference of diurnal warming between 0- and 1-m depths in the model is found because of the vertical temperature gradient in the upper 1 m (Fig. 16). Hence, the further quantitative comparison of individual diurnal warming may not be useful.

Since the model is able to simulate the realistic diurnal warming, it is useful to describe its spatial pattern and to compare with the surface forcing fields. Although overall spatial variation of the diurnal warming in the tropics can be described by the satellite-derived SST (e.g., Gentemann et al. 2003; Stuart-Menteth et al. 2003), its spatial and temporal resolutions are still not sufficient to fully describe the diurnal warming amplitude in the specific region and period such as the suppressed phase of the MJO. Figure 17a shows the average amplitude of the diurnal warming during the suppressed phase for the entire tropical Indian Ocean. Here, the amplitude is defined as $\Delta T/2$ where ΔT is the difference between the maximum and minimum SST within 24 h. The large diurnal warming is found near the equator and off-equatorial areas in the Arabian Sea. The amplitude exceeds 0.7°C around 0°–3°S, 80°–90°E and near the coast of Africa in the Arabian Sea around 15°N.

Figures 17b and 17c show the average wind speed and surface shortwave radiation for the same period, respectively. The spatial pattern of wind speed is quite similar to that of diurnal warming amplitude. The strong diurnal warming occurs in the areas where the average wind speed is less than 3 m s^{-1}. On the other hand, the spatial pattern of shortwave radiation is not similar to the diurnal warming amplitude. While shortwave radiation is much larger in the north of 10°N in the Bay of Bengal and Arabian Sea than near the equator, the strong diurnal warming is found mostly near the equator. This indicates that calm wind condition during the suppressed phase is mostly responsible for the observed large diurnal warming.

4. Summary and discussion

While COAMPS has been widely used in simulating a variety of atmospheric and oceanic phenomena in many locations (e.g., Pullen et al. 2003; Hsu et al. 2007; Jensen et al. 2011; Small et al. 2012), the simulation of oceanic and atmospheric variability associated with the MJO has not been evaluated and reported yet in past studies. This study compares the COAMPS MJO simulation with in situ and satellite observations over the tropical Indian Ocean. The primary focus is on the surface wind and upper-ocean variability produced by the MJO. The model was integrated for the period 1 March–30 April 2009 when an active episode of large-scale convection associated with the MJO passed eastward across the tropical Indian Ocean. The results demonstrate that COAMPS is able to simulate surface winds, oceanic equatorial jet, SST, and mixed layer evolution associated with the MJO reasonably well. In particular, strong eastward jet in the equatorial Indian Ocean during the active phase of the MJO is well simulated.

The COAMPS simulation validated by in situ observations is then used to describe large-scale variability of surface winds and upper-ocean currents. Strong westerly winds are centered around 3°S, 80°–85°E during the active phase, which are associated with the cyclonic circulation in the Bay of Bengal. The spatial pattern of winds is quite similar to that from NOGAPS, the

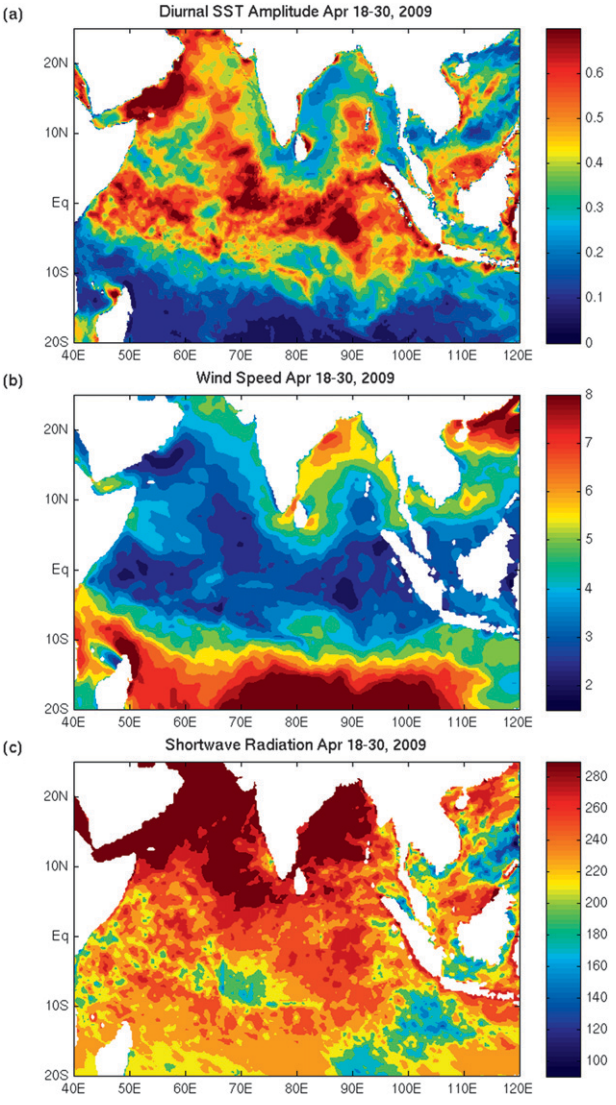

FIG. 17. (a) The average amplitude of SST diurnal cycle for the period 18–30 Apr 2009 (see text for the detail). (b) Average wind speed for the period 18–30 Apr 2009. (c) As in (b), but for surface shortwave radiation.

NCEP–NCAR reanalysis, and QuikSCAT, but the strength of the wind is significantly different between the datasets. Strong equatorial jets with the large zonal extent (60°E–the eastern boundary) are generated. The strongest zonal jets are located around 80°–90°E, which are associated with the strong meridional convergence.

To examine the sensitivity of the model results to the horizontal resolution of the atmospheric component, COAMPS is integrated for the same period and boundary conditions without the high-resolution nested grid in the central Indian Ocean. The comparison between the two experiments indicates that strong equatorial jets associated with the MJO is sensitive to the horizontal resolution of the atmospheric component of COAMPS. The westerlies during the active phase of the MJO are significantly weaker in the low-resolution model, and they generate eastward equatorial jet, which is about 20% weaker. The error of the equatorial jet influences upper-ocean salinity and temperature. In particular, upper-ocean salinity in the central equatorial Indian Ocean is largely affected because of the large zonal gradient of near-surface salinity.

Our results also indicate that the models used in the global ocean nowcast/forecast system such as NCOM do not always realistically simulate strong equatorial jets associated with the MJO partly because surface winds derived from the global atmospheric analysis (e.g., NOGAPS) used to force the model are not sufficiently accurate. This study suggests that the use of higher horizontal resolution with explicit moist physics in atmospheric models can largely improve the simulation of the equatorial currents associated with the MJO.

Since the ocean component of COAMPS used in this study employs exceptionally fine vertical spacing in the upper 10 m, the diurnal warming during the suppressed phase of the MJO is well represented by the model. The comparison with the in situ data indicates that large diurnal SST variations in the central Indian Ocean during the suppressed phase of the MJO are well simulated by COAMPS. The spatial pattern of the diurnal warming amplitude is described, and compared with the surface forcing fields. The spatial variation of wind speed is quite similar to that of the diurnal warming, and thus extremely weak winds during the suppressed phase of the MJO are mostly responsible for the large diurnal SST variations.

While this study primarily focuses on the evaluation of the model performance in simulating surface wind and ocean variability and its sensitivity to the model resolution, other atmospheric variability such as cloud variation, convection, and precipitation needs to be evaluated based on thorough analyses. Such model diagnoses are part of our ongoing and future research. After the full validation of COAMPS simulations for atmospheric and oceanic variability associated with the MJO, a variety of air–sea coupled processes important for its initiation and propagation (e.g., Flatau et al. 1997; Wang and Xie 1998; Kemball-Cook et al. 2002; Gribble-Verhagen and Roundy 2010) could be further investigated. For example, a meridional gradient of anomalous SST (more cooling near the equator) and zonal SST gradient near the eastern boundary during the active phase (Fig. 9) could influence winds and atmospheric convection. The impact of diurnal warming during the suppressed phase on the moisture variation and atmospheric convection could also be examined since the model can well represent the diurnal SST variation.

Although the MJO event in spring 2009, in which the associated ocean variation is relatively well monitored by the RAMA buoy, is quite suitable for the model validation in this study, the comparison with model simulations for other MJO events, which are well observed by in situ measurements, would be useful. During the recent field campaign: Dynamics of the Madden–Julian oscillation (DYNAMO; http://www.eol.ucar.edu/projects/dynamo), a substantial amount of data in the upper ocean and atmosphere have been collected in the central Indian Ocean, and the data are expected to be available in the near future. As thorough analyses of DYNAMO datasets will be conducted by many investigators in the next few years, COAMPS will hopefully help identify key processes for the MJO initiation through the model–data comparison and providing a tool for the analysis of its physical processes and dynamics.

Acknowledgments. The TAO Project Office of NOAA/PMEL provided the RAMA buoy time series data. QuikSCAT wind data are produced by Remote Sensing Systems. NCEP–NCAR reanalysis data are provided by the NOAA/OAR/ESRL PSD. We appreciate the effort of Tim Cambell and Travis Smith for the improvement of COAMPS and assistance for model experiments. Jerome Schmidt and Ming Liu contributed to the improvement of moist physics and radiation scheme in COAMPS. This research is supported by 6.1 project ''The Influence of Atmosphere Ocean Interaction on MJO Development and Propagation'' (Program Element 601153N) sponsored by the Office of Naval Research. Toshiaki Shinoda is also supported by NOAA/CPO MAPP and ESS programs.

REFERENCES

Barron, C. N., A. B. Kara, H. E. Hurlburt, C. Rowley, and L. F. Smedstad, 2004: Sea surface height predictions from the Global Navy Coastal Ocean Model (NCOM) during 1998–2001. *J. Atmos. Oceanic Technol.,* **21,** 1876–1894.

——, ——, P. J. Martin, R. C. Rhodes, and L. F. Smedstad, 2006: Formulation, implementation and examination of vertical coordinate choices in the global Navy Coastal Ocean Model (NCOM). *Ocean Modell.,* **11,** 347–375, doi:10.1016/j.ocemod.2005.01.004.

Bellenger, H., and J.-P. Duvel, 2009: An analysis of tropical ocean diurnal warm layers. *J. Climate,* **22,** 3629–3646.

Blumberg, A. F., and G. L. Mellor, 1987: A description of a three-dimensional coastal ocean circulation model. *Three-Dimensional Coastal Ocean Models,* N. Heaps, Ed., Amer. Geophys. Union, 1–16.

Chen, S., and Coauthors, 2003: COAMPS version 3 model description. NRL Publ. NRL/PU/7500-03-448, May 2003, 143 pp.

——, T. J. Campbell, H. Jin, S. Gaberšek, R. M. Hodur, and P. Martin, 2010: Effect of two-way air–sea coupling in high and low wind speed regimes. *Mon. Wea. Rev.,* **138,** 3579–3602.

——, ——, S. Gaberšek, H. Jin, and R. M. Hodur, 2011: Next generation air–ocean–wave Coupled Ocean/Atmosphere Mesoscale Prediction System (COAMPS). NRL review, 9 pp. [Available online at http://www.nrl.navy.mil/research/nrl-review/.]

Daley, R., and E. Barker, 2001: NAVDAS: Formulation and diagnostics. *Mon. Wea. Rev.,* **129,** 869–883.

Fairall, C., E. F. Bradley, D. P. Rogers, J. B. Edson, and G. S. Young, 1996: The TOGA COARE bulk flux algorithm. *J. Geophys. Res.,* **101,** 3747–3764.

Flatau, M., P. J. Flatau, P. Phoebus, and P. P. Niller, 1997: The feedback between equatorial convection and local radiative and evaporative processes: The implications for intraseasonal oscillations. *J. Atmos. Sci.,* **54,** 2373–2386.

Fox, D. N., W. J. Teague, C. N. Barron, M. R. Carnes, and C. M. Lee, 2002: The Modular Ocean Data Analysis System (MODAS). *J. Atmos. Oceanic Technol.,* **19,** 240–252.

Gentemann, C. L., C. J. Donlon, A. C. Stuart-Menteth, and F. J. Wentz, 2003: Diurnal signals in satellite sea surface temperature measurements. *Geophys. Res. Lett.,* **30,** 1140, doi:10.1029/2002GL016291.

Goerss, J. S., and P. A. Phoebus, 1992: The Navy's operational atmospheric analysis. *Wea. Forecasting,* **7,** 232–249.

Gribble-Verhagen, L., and P. E. Roundy, 2010: Analysis of apparent coupling between an oceanic Kelvin wave and atmospheric convection during the winter of 1986/87. *J. Climate,* **23,** 6352–6364.

Grunseich, G., B. Subrahmanyam, and A. Arguez, 2011: Influence of the Madden-Julian Oscillation on sea surface salinity in the Indian Ocean. *Geophys. Res. Lett.,* **38,** L17605, doi:10.1029/2011GL049047.

Han, W., J. P. McCreary, and K. E. Kohler, 2001: Influence of P-E and Bay-of-Bengal rivers on dynamics, thermodynamics, and mixed-layer physics in the Indian Ocean. *J. Geophys. Res.,* **106,** 6895–6916.

——, T. Shinoda, L.-L. Fu, and J. P. McCreary, 2006: Impact of atmospheric intraseasonal oscillations on the Indian Ocean dipole. *J. Phys. Oceanogr.,* **36,** 670–690.

Hodur, R. M., 1997: The Naval Research Laboratory's Coupled Ocean/Atmosphere Mesoscale Prediction System (COAMPS). *Mon. Wea. Rev.,* **125,** 1414–1430.

Hogan, T. F., and T. E. Rosmond, 1991: The description of the Navy Operational Global Atmospheric System's spectral forecast model. *Mon. Wea. Rev.,* **119,** 1786–1815.

Hsu, H.-M., L.-Y. Oey, W. Johnson, C. Dorman, and R. Hodur, 2007: Model wind over the central and Southern California coastal ocean. *Mon. Wea. Rev.,* **135,** 1931–1944.

Hung, M.-P., J.-L. Lin, W. Wang, D. Kim, T. Shinoda, and S. J. Weaver, 2013: MJO and convectively coupled equatorial waves simulated by CMIP5 climate models. *J. Climate,* in press.

Jensen, T. G., 2001: Arabian Sea and Bay of Bengal exchange of salt and tracers in an ocean model. *Geophys. Res. Lett.,* **28** (20), 3967–3970.

——, T. J. Campbell, R. A. Allard, R. J. Small, and T. A. Smith, 2011: Turbulent heat fluxes during an intense cold-air outbreak over the Kuroshio Extension Region: Results from a high-resolution coupled atmosphere–ocean model. *Ocean Dyn.,* **61,** 657–674, doi:10.1007/s10236-011-0380-0.

Kain, J. S., and J. M. Fritsch, 1990: A one-dimensional entraining/detraining plume model and its application in convective parameterization. *J. Atmos. Sci.,* **47,** 2784–2802.

——, and ——, 1993: Convective parameterization for mesoscale models: The Kain-Fritsch scheme. *The Representation of Cumulus Convection in Numerical Models, Meteor. Monogr.,* No. 46, Amer. Meteor. Soc., 165–170.

Kalnay, E., and Coauthors, 1996: The NCEP/NCAR 40-Year Reanalysis Project. *Bull. Amer. Meteor. Soc.,* **77,** 437–471.

Kemball-Cook, S., B. Wang, and X. H. Fu, 2002: Simulation of the intraseasonal oscillation in the ECHAM-4 model: The impact of coupling with an ocean model. *J. Atmos. Sci.,* **59,** 1433–1453.

Kessler, W. S., 2005: The oceans. *Intraseasonal Variability in the Atmosphere-Ocean Climate System,* W. K. M. Lau and D. E. Waliser, Eds., Praxis, 175–222.

——, and R. Kleeman, 2000: Rectification of the Madden–Julian Oscillation into the ENSO cycle. *J. Climate,* **13,** 3560–3575.

——, M. J. McPhaden, and K. M. Weickmann, 1995: Forcing of intraseasonal Kelvin waves in the equatorial Pacific Ocean. *J. Geophys. Res.,* **100,** 10 613–10 631.

Krishnamurti, T. N., D. K. Osterhof, and A. V. Mehta, 1988: Air–sea interaction on the time scale of 30 to 50 days. *J. Atmos. Sci.,* **45,** 1304–1322.

Liebmann, B., and C. A. Smith, 1996: Description of a complete (interpolated) outgoing longwave radiation dataset. *Bull. Amer. Meteor. Soc.,* **77,** 1275–1277.

Lin, J.-L., and Coauthors, 2006: Tropical intraseasonal variability in 14 IPCC AR4 climate models. Part I: Convective signals. *J. Climate,* **19,** 2665–2690.

Lukas, R., and E. Lindstrom, 1991: The mixed layer of the western equatorial Pacific Ocean. *J. Geophys. Res.,* **96** (S01), 3343–3357.

Madden, R. A., and P. R. Julian, 1972: Description of global-scale circulation cells in the tropics with a 40–50 day period. *J. Atmos. Sci.,* **29,** 1109–1123.

——, and ——, 1994: Observations of the 40–50-day tropical oscillation—A review. *Mon. Wea. Rev.,* **122,** 814–837.

Maes, C., J. Picaut, and S. Belamari, 2005: Importance of salinity barrier layer for the buildup of El Niño. *J. Climate,* **18,** 104–118.

Martin, P. J., 2000: A description of the Navy Coastal Ocean mode version 1.0. NRL Rep. NRL/FR/7322-00-9962, Naval Research Laboratory, Stennis Space Center, MS, 42 pp.

——, J. W. Book, and J. D. Doyle, 2006: Simulation of the northern Adriatic circulation during winter 2003. *J. Geophys. Res.,* **111,** C03S12, doi:10.1029/2006JC003511.

McPhaden, M. J., and X. Yu, 1999: Equatorial waves and the 1997-98 El Niño. *Geophys. Res. Lett.,* **26** (19), 2961–2964.

——, and Coauthors, 2009: RAMA: The Research Moored Array for African–Asian–Australian Monsoon Analysis and Prediction. *Bull. Amer. Meteor. Soc.,* **90,** 459–480.

Pullen, J., J. D. Doyle, R. Hodur, A. Ogston, J. W. Book, H. Perkins, and R. Signell, 2003: Coupled ocean-atmosphere nested modeling of the Adriatic Sea during winter and spring 2001. *J. Geophys. Res.,* **108,** 3320, doi:10.1029/2003JC001780.

Ralph, E. A., K. Bi, and P. P. Niiler, 1997: A Lagrangian description of the western equatorial Pacific response to the wind burst of December 1992. *J. Climate,* **10,** 1706–1721.

Rosmond, T. E., 1992: The design and testing of the Navy Operational Global Atmospheric Prediction System. *Wea. Forecasting,* **7,** 262–272.

Roundy, P. E., and G. N. Kiladis, 2006: Observed relationships between oceanic Kelvin waves and atmospheric forcing. *J. Climate,* **19,** 5253–5272.

Rutledge, S. A., and P. V. Hobbs, 1983: The mesoscale and microscale structure and organization of clouds and precipitation in midlatitude cyclones. VIII: A model for the ''seeder-feeder'' process in warm-frontal rainbands. *J. Atmos. Sci.,* **40,** 1185–1206.

Saji, N. H., B. N. Goswami, P. N. Vinayachandran, and T. Yamagata, 1999: A dipole mode in the tropical Indian Ocean. *Nature,* **401,** 360–363.

Schott, F., and J. P. McCreary, 2001: The monsoon circulation of the Indian Ocean. *Prog. Oceanogr.,* **51,** 1–123.

Sengupta, D., R. Senan, B. N. Goswami, and J. Vialard, 2007: Intraseasonal variability of equatorial Indian Ocean zonal currents. *J. Climate,* **20,** 3036–3055.

Shinoda, T., 2005: Impact of the diurnal cycle of solar radiation on intraseasonal SST variability in the western equatorial Pacific. *J. Climate,* **18,** 2628–2636.

——, and R. Lukas, 1995: Lagrangian mixed layer modeling of the western equatorial Pacific. *J. Geophys. Res.,* **100,** 2523–2541.

——, and H. H. Hendon, 1998: Mixed layer modeling of intraseasonal variability in the tropical western Pacific and Indian Oceans. *J. Climate,* **11,** 2668–2685.

——, and ——, 2001: Upper ocean heat budget in response to the Madden–Julian Oscillation in the western equatorial Pacific. *J. Climate,* **14,** 4147–4165.

——, and W. Han, 2005: Influence of Indian Ocean dipole on atmospheric subseasonal variability. *J. Climate,* **18,** 3891–3909.

——, H. H. Hendon, and J. Glick, 1998: Intraseasonal variability of surface fluxes and sea surface temperature in the tropical western Pacific and Indian Ocean. *J. Climate,* **11,** 1685–1702.

——, ——, and ——, 1999: Intraseasonal surface fluxes in the tropical western Pacific and Indian Ocean from NCEP reanalyses. *Mon. Wea. Rev.,* **127,** 678–693.

——, P. E. Roundy, and G. N. Kiladis, 2008: Variability of intraseasonal Kelvin waves in the equatorial Pacific Ocean. *J. Phys. Oceanogr.,* **38,** 921–944.

Small, R. J., S. Carniel, T. Campbell, J. Teixeira, and R. Allard, 2012: The response of the Ligurian and Tyrrhenian Sea to a summer Mistral event: A coupled atmosphere-ocean approach. *Ocean Modell.,* **48,** 30–44, doi:10.1016/j.ocemod.2012.02.003.

Soloviev, A. V., and R. Lukas, 1997: Observation of large diurnal warming events in the near-surface layer of the western equatorial Pacific warm pool. *Deep-Sea Res.,* **44,** 1055–1076.

Sprintall, J., and M. Tomczak, 1992: Evidence of the barrier layer in the surface layer of the tropics. *J. Geophys. Res.,* **97** (C5), 7305–7316.

Stuart-Menteth, A. C., I. S. Robinson, and P. G. Challenor, 2003: A global study of diurnal warming using satellite-derived sea surface temperature. *J. Geophys. Res.,* **108,** 3155, doi:10.1029/2002JC001534.

Subramanian, A. C., M. Jochum, A. J. Miller, R. Murtugudde, R. B. Neale, and D. E. Waliser, 2011: The Madden–Julian oscillation in CCSM4. *J. Climate,* **24,** 6261–6282.

Waliser, D. E., R. Murtugudde, and L. Lucas, 2003: Indo-Pacific ocean response to atmospheric intraseasonal variability. Part I: Austral summer and the Madden-Julian oscillation. *J. Geophys. Res.,* **108,** 3160, doi:10.1029/2002JC001620.

Wang, B., and X. Xie, 1998: Coupled modes of the warm pool climate system. Part I: The role of air–sea interaction in maintaining Madden–Julian Oscillation. *J. Climate,* **11,** 2116–2135.

Weaver, S. J., W. Wang, M. Chen, and A. Kumar, 2011: Representation of MJO variability in the NCEP Climate Forecast System. *J. Climate,* **24,** 4676–4694.

Weller, R. A., and S. P. Anderson, 1996: Surface meteorology and air–sea fluxes in the western equatorial Pacific warm pool during the TOGA Coupled Ocean–Atmosphere Response Experiment. *J. Climate,* **9,** 1959–1990.

Wheeler, C. M., and H. H. Hendon, 2004: An all-season real-time multivariate MJO index: Development of an index for monitoring and prediction. *Mon. Wea. Rev.,* **132,** 1917–1932.

Woolnough, S. J., F. Vitart, and M. A. Balmaseda, 2007: The role of the ocean in the Madden–Julian Oscillation: Implications for MJO prediction. *Quart. J. Roy. Meteor. Soc.,* **133,** 117–128.

Yoshida, K., 1959: A theory of the Cromwell current and of the equatorial upwelling—An interpretation in a similarity to a coastal circulation. *J. Oceanogr. Soc. Japan,* **15,** 159–170.

Zhang, C., 1996: Atmospheric intraseasonal variability at the surface in the tropical western Pacific Ocean. *J. Atmos. Sci.,* **53,** 739–758.